AIChE WILEY InterScience DISCOVER SOMETHING GREAT

FLUID MECHANICS AND TRANSPORT PHENOMENA

Role of Various Elliptical Shapes for Efficient Microwave Processing of Materials

Tanmay Basak
Dept. of Chemical Engineering, Indian Institute of Technology, Madras, Chennai 600 036, India

DOI 10.1002/aic.11160
Published online April 13, 2007 in Wiley InterScience (www.interscience.wiley.com).

A detailed theoretical analysis has been carried out to assess the role of various elliptical shapes/cross sections on microwave heating of 2-D cylinders for beef and oil samples. Two types of elliptical cross sections are considered as type A (ellipse with major axis along the horizontal plane), and type B (ellipse with minor axis along the horizontal plane.) A preliminary analysis on microwave heating of samples has been shown via average power within a sample vs. sample radius of circular cross section for beef and oil samples. Several regimes (I–III) based on small and large radius for circular cross sections have been selected. The effect of elliptical shapes for type A and B configurations has been studied initially via average power vs. aspect ratio distributions for various regimes. The grayscale images of power absorption have been analyzed further for elliptical cross section with varying aspect ratios for regimes I–III where aspect ratio and types of configuration are shown to influence spatial power absorptions. The detailed temperature profiles have also been shown to illustrate the role of elliptical shapes on uniform heating and thermal runaway. Depending on the material dielectric properties and sample dimension, either type A or B or both configuration has been recommended. © 2007 American Institute of Chemical Engineers *AIChE J,* 53: 1399–1412, 2007
Keywords: microwave, cylinders, elliptical shapes

Introduction

Microwaves have a wide range of applications in various industries such as heating and thawing of materials, food processing, drying, sintering of ceramics, polymer processing and many more.[1–9] Microwaves have received significant attention due to interaction of waves within materials, resulting in volumetric generation of heat. The volumetric heating is in general spatially nonuniform due to dipolar interaction within the medium. Increasing demands in industries and complexities in physical process led to large amounts of research for efficient processing of materials with microwaves.

A number of experimental works have been carried out on enhanced material processing rates corresponding to maxima in microwave power or "resonances". It may be noted that resonance corresponds to constructive interference of traveling waves within the medium. Ohlsson and Risman[10] carried out experimental studies on microwave heating at 2,450 MHz for spherical and cylindrical samples. Maxima in power absorption were observed at the center of the sample for spheres and cylinders with diameters in the range of 2–6 cm and 1.8–3.5 cm, respectively. Massoudi et al.[11,12] studied the average power absorption in homogeneous and multilayered cylindrical samples by varying the frequency of radiation for a sample with fixed diameter. Their predictions showed the presence of resonances for the multilayered samples only. Ruppin[13] predicted resonance in the average power absorption for cylinders in the presence of reflecting surfaces. A greater effect in resonances was observed in spheres. Weil[1] predicted average power over the frequency range for spheres of radii 3.3 cm and 6 cm, where strong resonances were observed when the frequency was varied. Schlunder[14] studied

T. Basak's e-mail address is: tanmay@iitm.ac.in.

the influence of resonances in power on drying rates of liquid filled spheres. Various experimental studies on efficient material processing form the basis of theoretical studies especially microwave heating of 1-D slab and 2-D cylinders.

Ayappa et al.[15,2] carried out theoretical and numerical studies on microwave heating of 1-D slabs and 2-D cylinders, and they observed a greater heating rate for thinner samples, while heating occurs primarily at the incident face for thicker samples. Basak and Ayappa[5,6,16] carried out microwave thawing for 1-D slabs and 2-D cylinders of pure and multicomponent samples, and they observed a greater melting rate during resonances. They also observed multiple melting fronts for thinner cylinders corresponding to greater thawing rates. The counterintuitive situation, such as thicker samples taking less time to thaw than thinner samples in presence of resonance, was recently analyzed by Basak.[17] Ayappa et al.[18] and Ayappa[19] carried out detailed analysis on resonances of microwave power for 1-D slabs and 2-D cylinders, and they found that the resonances in average power occur for fixed sample dimensions following suitable relationships. Later, Basak and Kumaran[20] analyzed resonances with material invariant characteristics. A detailed analysis on resonances for heating of emulsions are also recently addressed by Basak.[21]

Resonances or maxima in microwave power enhances material processing rate, whereas there are also minima in power absorption corresponding to destructive interference of traveling waves, which slows down the material processing rate with microwaves. Microwaves are wastefully used due to minima in power absorption for specific sample dimensions. The interference between traveling waves may be altered via changing the shapes of materials. 2-D materials with circular cross section incident with microwaves may be considered, and it may be interesting to analyze the enhancement and/or distribution of microwave power via systematic deformation of circular cross section to elliptical with various types. Role of various elliptical shapes also gives some ideas of realistic shapes and the concept on enhancement or efficient heating policy influenced by various such shapes is yet to appear in the literature.

Here, a detailed analysis on microwave heating has been carried out for various elliptical shapes: type A and type B. Note that, type A refers to ellipse with major axis along the horizontal direction and type B corresponds to ellipse with minor axis along the horizontal direction. The governing equations for electric field and temperature with the appropriate boundary conditions are solved using finite element method, which is also advantageous for solving equations in any arbitrary domain. The electric fields are governed by Maxwell's equation with various radiation boundary conditions. The radiation boundary conditions are based on the circular domain, and, therefore, a superficial circular domain has been considered around the ellipse such that interface elements at the elliptical boundary satisfy the electric field continuity. The energy balance equation with a microwave power term is solved to predict temperature dynamics. The effect of elliptical shape has been illustrated for the cases with and without resonances, as well as for large sample dimensions. The detailed analysis of temperature dynamics has been utilized to predict efficient heating strategy, and a recommendation has been made on suitability of either type A or type B shape for various aspect ratios depending on sample size and dielectric properties. The analysis has been done with two representative food materials corresponding to high- and low-dielectric losses (beef and oil).

Modeling and simulation

Evaluation of Microwave Power and Temperature. Microwaves are assumed to be incident normally on the infinite cylinder as shown in Figure 1a. We consider various cross sections of cylinders as horizontal ellipse (major axis is along the horizontal plane; type (A)), vertical ellipse (minor axis is along the horizontal plane; type (B)) and circles as seen in Figure 1b. The incident microwave is a uniform plane wave, with the electric and magnetic components varying in intensity only in the direction of wave propagation (z axis). The wave propagation due to electric field, E_x, is governed by[2]

$$\nabla^2 E_x + k^2 E_x = 0 \tag{1}$$

where E_x varies in the y–z plane only as seen in Figure 1a, and the propagation constant

$$k = \frac{\omega}{c}\sqrt{\kappa' + i\kappa''} \tag{2}$$

depends on the dielectric constant, κ' and the dielectric loss κ''. Note that, $\omega = 2\pi f$, where f is the frequency of the electromagnetic wave, and c is the velocity of light. The propa-

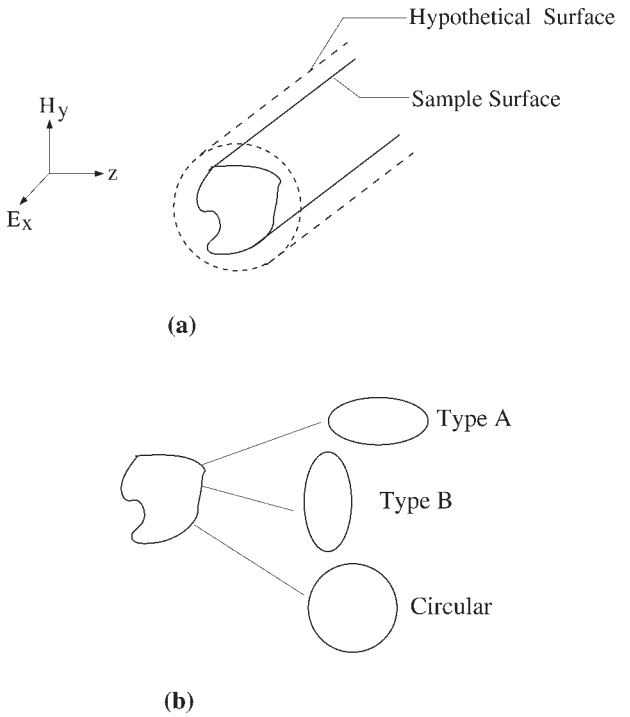

Figure 1. (a) 2-D cylinder with arbitrary cross section exposed to plane electromagnetic waves, and (b) three types of cross sections.

The dotted surface in (a) denotes the hypothetical surface with circular cross section.

gation constant in Eq. 2 based on two length scales (wavelength and penetration depth), may also be represented as

$$k = (2\pi/\lambda_m) + i(1/D_p) \tag{3}$$

The penetration depth D_p, and wavelength of radiation in the medium λ_m are related to κ' and κ'' in the following manner

$$D_p = \frac{c}{\sqrt{2}\pi f\left[\kappa'\left(\sqrt{1+\left(\frac{\kappa''}{\kappa'}\right)^2}-1\right)\right]^{1/2}} \tag{4}$$

and

$$\lambda_m = \frac{c\sqrt{2}}{f\left[\kappa'\left(\sqrt{1+\left(\frac{\kappa''}{\kappa'}\right)^2}+1\right)\right]^{1/2}} \tag{5}$$

The microwave propagation within a lossy dielectric medium is generally associated with heat generation due to dissipation of electric energy into heat. The heat transport may be modeled using following assumptions. The material is assumed to have constant thermal properties without any change in phase throughout the heating process. The analysis is based on the assumption of zero shrinkage, that is, the food sample do not experience a time-dependent change in volume during heating. The shrinkage effect is negligible based on the previous work by Fowler and Bejan.[22] The natural convection within the material is also assumed to be neglected. The heat transport within a sample due to volumetric absorption of microwave power, q is governed by the energy balance equation

$$\rho C_p \frac{\partial T}{\partial t} = k\nabla^2 T + q \tag{6}$$

where ρC_p is the specific heat per unit volume, k is the thermal conductivity and

$$q = \frac{1}{2}\omega\varepsilon_0\kappa'' E_x E_x^* \tag{7}$$

where ε_0 is the free space permittivity. The dielectric loss, κ'' may be assumed as a constant within a sample. The overall heating effect may be represented by the average power, which may be obtained by integrating the power across the domain

$$q_{av} = \frac{1}{A_c}\int_{\Gamma_1} q(\Omega)d\Omega \tag{8}$$

Here Γ_1 denotes the outer surface of the sample, and A_c is the cross sectional area of the sample. Various computational domains are shown in Figures 2a–d. It may be noted that a hypothetical circular domain (see Figure 1a and Figures 2a–d) is required to impose the radiation boundary condition (RBC) to solve Maxwell's equation (Eq. 1) as discussed next.

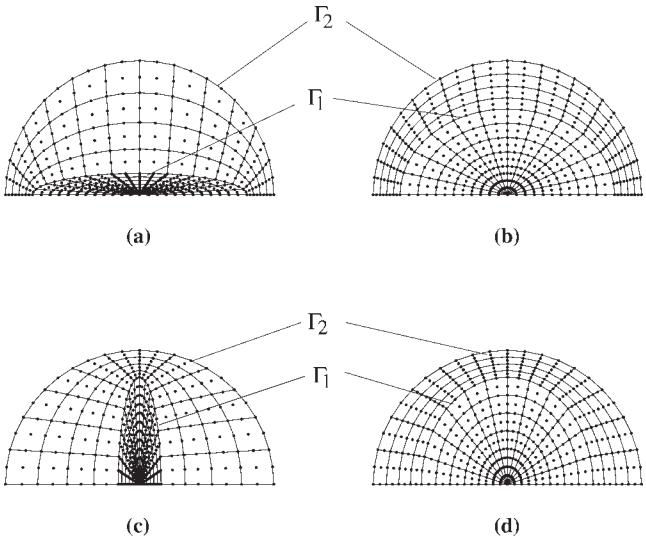

Figure 2. Computational half domain and finite element grids with biquadratic elements of type A and type B cross sections.

Here (a)–(b) correspond to small ($a = 0.2$) and large ($a = 0.8$) aspect ratios, respectively for type A cross section, and (c)–(d) correspond to small ($a = 0.2$), and large ($a = 0.8$) aspect ratios, respectively, for type B cross section. Note that, Γ_1 denotes the outer surface of the elliptical domain and Γ_2 denotes the hypothetical circular surface.

Using the dimensionless variables

$$u_x = \frac{E_x}{E_0} \quad \text{and} \quad \nabla^* = R_h\nabla$$

Eq. 1 reduces to

$$\nabla^{*2}u_x + \gamma^2 u_x = 0 \tag{9}$$

where u_x is the electric field intensity, $\gamma = \frac{R_h\omega}{c}\sqrt{\kappa' + i\kappa''}$ is the propagation constant, and R_h is the radius of the hypothetical circular domain. Substituting the complex field variable $u_x = v_x + iw_x$ into Eq. 9, and equating the real and imaginary components, we get

$$\nabla^{*2}v_x + \chi_1 v_x - \chi_2 w_x = 0 \tag{10}$$

and

$$\nabla^{*2}w_x + \chi_2 v_x + \chi_1 w_x = 0 \tag{11}$$

with $\chi_1 = \frac{R_h^2\omega^2}{c^2}\kappa'$ and $\chi_2 = \frac{R_h^2\omega^2}{c^2}\kappa''$.

Due to uniform plane wave propagation with the electric field E_x varying in $y-z$ plane, the governing equations may be solved for the half domain represented by Figures 2a–d. For uniform plane waves incident on a sample, some of the radiation is scattered, and the rest is absorbed. The domain of such problems is unbounded, and many methods have been devised to impose boundary conditions that minimize the domain of analysis. For microwave heating situations, the absorbed field is of prime interest, and modeling studies also involve minimization of the space around the sample. The

suitable formulation for this situation is based on the exact RBC developed by Keller and Givoli[23] to study scattered field patterns. This boundary condition is imposed on the surface of the cylinder for samples with circular cross-section, and for other shapes, the boundary condition is imposed on a hypothetical cylindrical surface with circular cross section. Furthermore, this hypothetical cylindrical surface can be placed as close to the sample as desired. This method may be efficient for finite element analysis, as an element can be placed at the interface between the sample boundary (Γ_1) and hypothetical boundary in free space (Γ_2) (see Figures 2a–d).

Radiation boundary conditions (RBC) are used at the outer surface of the cylinder[2] (Γ_2; see Figures 2a–d).

$$\mathbf{n}\cdot\nabla^* v_x = \sum_{n=0}^{\infty} Re(C_n)\cos n\phi + \sum_{n=0}^{\infty} Re(D_n)\int_0^{2\pi} v_x(1,\phi')\cos n(\phi-\phi')d\phi' - \sum_{n=0}^{\infty} Im(D_n)\int_0^{2\pi} w_x(1,\phi')\cos n(\phi-\phi')d\phi' \quad (12)$$

and

$$\mathbf{n}\cdot\nabla^* w_x = \sum_{n=0}^{\infty} Im(C_n)\cos n\phi + \sum_{n=0}^{\infty} Im(D_n)\int_0^{2\pi} v_x(1,\phi')\cos n(\phi-\phi')d\phi' + \sum_{n=0}^{\infty} Re(D_n)\int_0^{2\pi} w_x(1,\phi')\cos n(\phi-\phi')d\phi' \quad (13)$$

with the coefficients

$$C_n = \frac{\varepsilon_n i^n \omega R_h}{c}\left[J_n'\left(\frac{\omega R_h}{c}\right) - J_n\left(\frac{\omega R_h}{c}\right)\frac{H_n^{(1)'}\left(\frac{\omega R_h}{c}\right)}{H_n^{(1)}\left(\frac{\omega R_h}{c}\right)}\right] \quad (14)$$

and

$$D_n = \frac{\omega R_h \delta_n H_n^{(1)'}\left(\frac{\omega R_h}{c}\right)}{c\pi H_n^{(1)}\left(\frac{\omega R_h}{c}\right)} \quad (15)$$

and

$$\varepsilon_n = \begin{cases} 1, & n=0; \\ 2, & \text{otherwise} \end{cases} \quad \text{and} \quad \delta_n = \begin{cases} 1/2, & n=0; \\ 1, & \text{otherwise} \end{cases} \quad (16)$$

In Eqs. 14 and 15, J_n and $H_n^{(1)}$ are the Bessel and Hankel functions of the first kind, respectively, and prime indicates the first derivatives.

Dimensionless form of the energy balance equation in the presence of microwave, Eq. 6 is

$$\overline{\rho C_p}\frac{\partial\theta}{\partial\tau} = \overline{k}\nabla^{*2}\theta + Q \quad (17)$$

where

$$\theta = \frac{T-T_\infty}{T_0},\quad \tau = \frac{\alpha_0 t}{R_h^2},\quad \overline{\rho C_p} = \frac{\rho C_p}{\rho_0 C_{p_0}},\quad \overline{k} = \frac{k}{k_0} \quad \text{and} \quad Q = \frac{R_h^2 q}{k_0 T_0}$$

Here ρ_0, C_{p_0}, k_0 and α_0 are the reference density, heat capacity, thermal conductivity and thermal diffusivity, respectively. The initial condition for the entire 2-D sample is

$$\theta(\tau=0) = \frac{T_0 - T_\infty}{T_0} = 0. \quad (18)$$

In the analysis, an insulated boundary condition is used as

$$-\mathbf{n}\cdot\overline{k}\nabla^*\theta = 0 \quad (19)$$

and the insulated boundary condition is maintained at the outer surface (Γ_1) of the sample. The insulated condition is imposed to analyze the heating effects due to heat generation only.

Simulation procedure

The electric field equations (Eqs. 10 and 11), and the energy balance equation (Eq. 17) are solved using the Galerkin finite element method. The symmetry of the microwave radiation with respect to $y = 0$ as shown in Figure 1, results in a temperature distribution, which is also symmetric with respect to $y = 0$. Hence, we solve the equations only in the upper-half of the cross section as shown in Figures 2a–d. Expanding the real (v_x) and imaginary components (w_x) of the electric field, and the temperature (θ) in a basis set $\{\psi\}$

$$v_x \approx \sum_{k=1}^{N} v_{x,k}\,\psi_k(y,z), \quad w_x \approx \sum_{k=1}^{N} w_{x,k}\,\psi_k(y,z) \quad \text{and} \quad \theta \approx \sum_{k=1}^{N}\theta_k\,\psi_k(y,z) \quad (20)$$

for

$$-1 \le y,z \le 1$$

the Galerkin finite element method yields the following nonlinear residual equations for Eqs. 10, 11, and 17, respectively

$$R_i^{(1)} = \sum_{k=1}^{N} v_{x,k}^{t+1}\int_\Omega\left[\frac{\partial\psi_i}{\partial y}\frac{\partial\psi_k}{\partial y} + \frac{\partial\psi_i}{\partial z}\frac{\partial\psi_k}{\partial z}\right]dy\,dz + \sum_{k=1}^{N} w_{x,k}^{t+1}\int_\Omega \chi_2\psi_i\psi_k\,dy\,dz - \sum_{k=1}^{N} v_{x,k}^{t+1}\int_\Omega \chi_1\psi_i\psi_k dy\,dz - \int_{\Gamma_2}\psi_i\,\mathbf{n}\cdot\nabla^* v_x^{t+1}d\Gamma \quad (21)$$

$$R_i^{(2)} = \sum_{k=1}^{N} w_{x,k}^{t+1} \int_\Omega \left[\frac{\partial \psi_i}{\partial y}\frac{\partial \psi_k}{\partial y} + \frac{\partial \psi_i}{\partial z}\frac{\partial \psi_k}{\partial z}\right] dy\, dz - \sum_{k=1}^{N} v_{x,k}^{t+1} \int_\Omega \chi_2 \psi_i \psi_k dy\, dz - \sum_{k=1}^{N} w_{x,k}^{t+1} \int_\Omega \chi_1 \psi_i \psi_k dy dz - \int_{\Gamma_2} \psi_i \mathbf{n} \cdot \nabla^* w_x^{t+1} d\Gamma \quad (22)$$

$$R_i^{(3)} = \sum_{k=1}^{N} \int_\Omega \overline{\rho C_p}\left(\frac{\theta_k^{t+1} - \theta_k^t}{\Delta\tau}\right)\psi_i \psi_k dy\, dz + \frac{1}{2}\left[F(\theta^{t+1}, v_x^{t+1}, w_x^{t+1}) + F(\theta^t, v_x^t, w_x^t)\right] \quad (23)$$

where

$$F(\theta^t, v_x^t, w_x^t) = \sum_{k=1}^{N} \theta_k^t \int_\Omega \bar{k}\left[\frac{\partial \psi_i}{\partial y}\frac{\partial \psi_k}{\partial y} + \frac{\partial \psi_i}{\partial z}\frac{\partial \psi_k}{\partial z}\right] dy\, dz - \int_{\Gamma_1} \psi_i \mathbf{n} \cdot \nabla^* \theta^t d\Gamma - \frac{R_h^2 \omega \varepsilon_0 E_0^2}{2 k_0 T_0} \times \int_\Omega \kappa'' \left[\left(\sum_k v_{x,k}^t \psi_k\right)^2 + \left(\sum_k w_{x,k}^t \psi_k\right)^2\right] \psi_i\, dy\, dz \quad (24)$$

and

$$i = 1 \ldots N \text{ and } t = \text{time index}$$

The gradients of the electric field in the surface integrals due to RBC of Eqs. 21 and 22, are evaluated using Eqs. 12 and 13. Evaluation of RBC for a half domain (Figures 2a–d) is discussed in an earlier work.[16] The residual equation for temperature (Eq. 23) has been shown for the interior domain bounded by Γ_1 (see Figures 2a–d). The outer nodes between Γ_2 and Γ_1 excluding the nodes at Γ_1 are maintained at ambient temperature. The nodes at Γ_1 are subjected to thermally insulated situation as indicated in the surface integral of Eq. 24. The continuity of electric field and temperature at the interface between the elliptical sample and hypothetical domain are automatically satisfied via the interfacial element. The finite element meshes, and the computational domain for the 2-D cylinder are shown in Figures 2a–d.

The unconditionally stable Crank-Nicholson algorithm, is used to discretize the time domain in Eq. 23, and biquadratic basis functions with three point Gaussian quadrature is used to evaluate the integrals in the residual equations. The nonlinear residual equations (Eqs. 21, 22 and 23) are solved using a Newton-Raphson procedure, to determine the coefficients of the expansions in Eq. 20 at each time step. At each time step, the linear ($3N \times 3N$) system solved is

$$\mathbf{J}\left(\mathbf{U}^{n,t+1}\right)\left[\mathbf{U}^{n,t+1} - \mathbf{U}^{n+1,t+1}\right] = \mathbf{R}\left(\mathbf{U}^{n,t+1}\right) \quad (25)$$

where n is the Newton iterate index, and t the time index. The elements of the Jacobian matrix, $\mathbf{J}(\mathbf{U}^{n,t+1})$ contains the derivatives of the residual equations with respect to the temperature (θ_j's), and electric field unknowns ($v_{x,j}$'s and $w_{x,j}$'s), and $\mathbf{R}(\mathbf{U}^{n,t+1})$ is the vector of residuals.

We have used nine node biquadratic elements with each element mapped using isoparametric mapping from $x - y$ to a unit square $\xi - \eta$ domain.[24] Correspondingly, the domain integrals in the residual equations are evaluated using nine node biquadratic basis functions in $\xi - \eta$ domain, using

$$x = \sum_{i=1}^{9} x_i \psi_i(\xi, \eta) \text{ and } y = \sum_{i=1}^{9} y_i \psi_i(\xi, \eta) \quad (26)$$

where $\psi_i(\xi,\eta)$ are the local biquadratic basis functions on the $\xi - \eta$ domain. At the center of the cylinder collapsed elements are used where three nodes share the co-ordinates at the origin.

Convergence tests were carried out and typically 120–144 biquadratic elements are used within the entire domain for all computations. The adaptive meshing has also been implemented and refined meshes are used for the elliptical domain specially with high-aspect ratios as seen in Figures 2a,c. The ratio between the radius of major axis of the ellipse (bounded by surface Γ_1), and the radius of the hypothetical circular surface (Γ_2) is chosen at 0.8, and typically 48 biquadratic elements are placed in the domain bounded by Γ_1 and Γ_2. Due to the lack of a good initial guess to begin the Newton scheme, a small time-step $\Delta t = 1 \times 10^{-4}$ s was used at the first time-step. Unless specified otherwise $\Delta t = 0.1$ s was used for subsequent steps. It was found that the maximum difference for the values of the unknowns at the nodes was less than 1% when the values were compared for 120 and 144 elements. Similarly the maximum difference was less than 1% when the results were compared for $\Delta t = 0.05$ s and 0.1 s.

The simulations are carried out for beef (with high-dielectric loss) and oil (with low dielectric loss) cylinders, which are exposed to the microwave radiation of intensity 1 W cm^{-2}. The sample is at 300 K during $t = 0$ s. The thermal and dielectric properties for beef and oil are given in Table 1.

The temperature and power contours of beef samples in 2-D circular domain with hypothetical surface is validated with the results without the hypothetical surface,[2] and the results are in well agreement. Initially, the heating studies are shown for cylinders with circular cross sections. The heating simulations are later extended for ellipses with various aspect ratios (a), where a is defined as the ratio between the minor radius (r_1) and major radius (r_2). The influence of various shapes of ellipse on microwave heating has been investigated for fixed area of the cross section, such that the radius (R) of the specific circular cross section, r_1 and r_2 are related with the relationship: $R = \sqrt{r_1 r_2}$.

Table 1. Thermal and Dielectric Properties are given for Oil and Raw Beef[15]

Material Property	Oil	Raw Beef
Heat capacity, C_p[W s kg^{-1} °C^{-1}]	2000	2510
Thermal conductivity, k[W m^{-1} °C^{-1}]	0.168	0.491
Density, ρ[kg m^{-3}]	900	1070
Dielectric constant (2450 MHz), κ'	2.80	43
Dielectric loss (2450 MHz), κ''	0.15	15

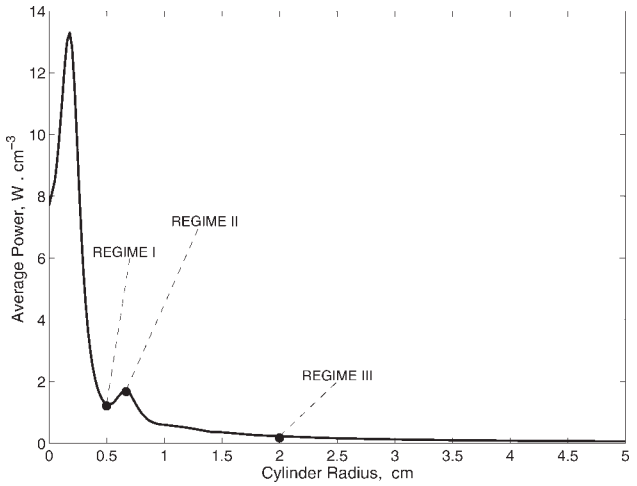

Figure 3. Average power (W · cm^{-3}) vs. cylinder radius (cm) for beef samples.

f = 2450 MHz, the incident microwave intensity at left face, I_0 = 1 W cm^{-2}. The regime I corresponds to minima in average power, regime II represents a maxima and regime III represents a large sample.

Results and Discussion

Microwave heating of beef samples

A preliminary case study on microwave heating of beef for cylinders with circular cross sections has been illustrated via average power vs. cylinder radius as shown in Figure 3, where the average power is obtained using Eq. 8. The average power exhibits several maxima, which are often referred as resonances.[18] The resonances occur at specific sample radius, which is a function of the wavelength within the sample based on the following relationship [18]

$$\frac{R}{\lambda_m} = 0.25n - 0.1285 \tag{27}$$

where $n = 1,2,\ldots$. Note that, the wavelength (λ_m), and penetration depth (D_p) for beef samples are 1.838 cm and 1.72 cm, respectively. The two primary maxima in average power occur at $R = 0.18$ and 0.67 cms, while the minima occur at $R = 0.5$ cm, and for $R \geq 2$ cm, the average power is found to decrease asymptotically. For the first resonance peak, the average power is quite large (approximately 13 W cm^{-3}), therefore, studies on enhancement of power with various elliptical cross sections may not be important. The influence of various elliptical cross sections would be investigated, especially for the three regimes I, II and III, corresponding to $R = 0.5$, 0.67 and 2 cms, respectively. It may be noted that for a circular cross section, regime I corresponds to minima in average power, regime II denotes maxima, and regime III denotes minima within a sample. In addition, regimes I and II correspond to smaller radius of circular cross section, and regime III represents a sample with large radius of cross section.

The influence of various shapes of elliptical cross sections is analyzed with a range of aspect ratios for types A and B configurations, where type A refers to the ellipse with major axis along the horizontal plane, and type B refers to the ellipse with minor axis along the horizontal plane, as illustrated in Figure 1b. A preliminary analysis on the influence of various shapes of elliptical cross section for microwave heating of 2-D cylinders has been illustrated via average power vs aspect ratio for regimes I, II and III, as seen in Figures 4a–c. In order to perform calculations, the cross sectional area for various aspect ratios of ellipses (types A and B) was assumed to be identical to the cross sectional area of the circular cylinder of a specific regime (Regime I or II or III).

Figure 4a illustrates the average power distributions for regime I corresponding to $R = 0.5$ cm. It has been observed that the average power is enhanced for both types A and B elliptical cross sections, and average power is found to decrease with aspect ratio (a) for both types of elliptical cross sections. It is interesting to note that for $a \leq 0.7$, the enhancement with type A cross section is larger than that with type B cross section. It may also be noted that, type A cross section would cause very high-enhancement of average power for small aspect ratios, and type B cross section corresponds to almost constant average power for $a \geq 0.7$. It is found that the average power is around 5.3 W cm^{-3} for $a = 0.1$ with type A cross section, whereas the average power is 1.48 W cm^{-3} for $a = 0.1$ with type B cross section. It may be noted that the average power is 1.27 W cm^{-3} for $a = 1$ with both types of cross section.

Figure 4b illustrates the average power distributions for regime II with $R = 0.67$ cm. It is interesting to note that the average power is high (2.14 W cm^{-3}) for $a = 0.1$ with type

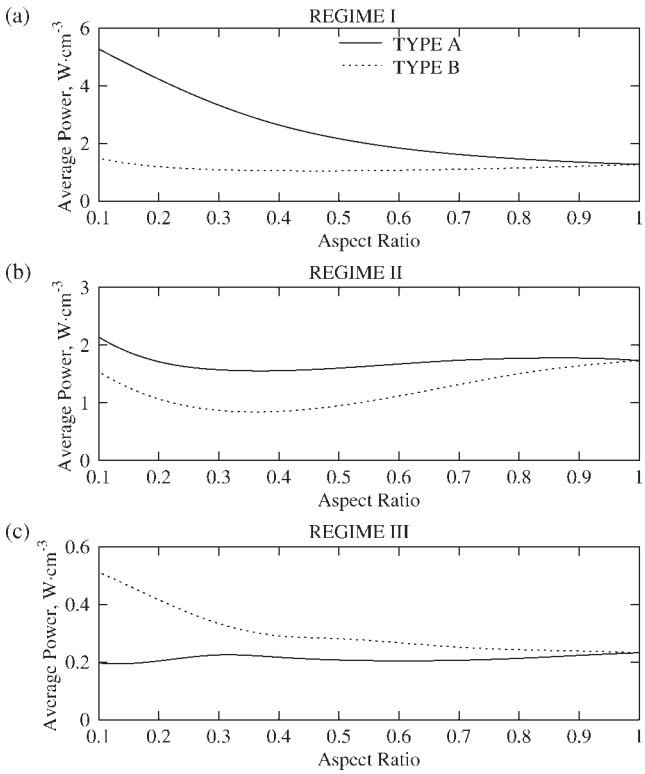

Figure 4. Average power (W · cm^{-3}) vs. aspect ratio for beef samples with (a) regime I, (b) regime II, and (c) regime III.

f = 2450 MHz, the incident microwave intensity at left face, I_0 = 1 W cm^{-2}. The average power with type A cross section is larger than that with type B cross section for regimes I and II, whereas the average power with type B cross section is larger for regime III.

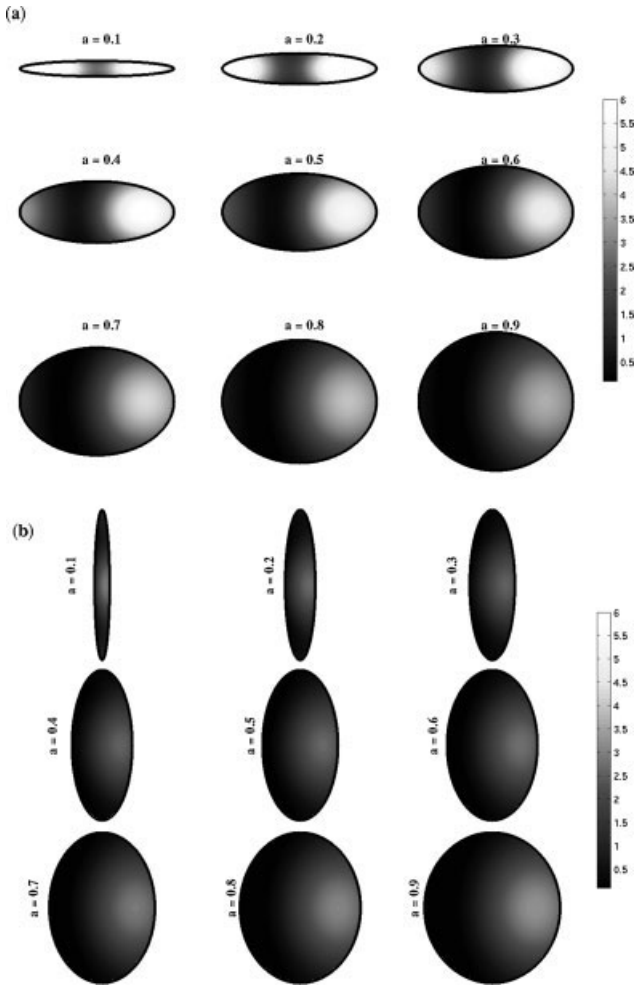

Figure 5. Grayscale colormap images of microwave power distributions in beef samples for various aspect ratios with (a) type A, (b) type B cross sections corresponding to regime I (R = 0.5 cm).

$f = 2450$ MHz, the incident microwave intensity at left face, $I_0 = 1$ W cm^{-2}. It may be noted that brighter regime denotes larger power distribution. Two strong bright regimes near the left and right faces are seen for type A cross section with small aspect ratios.

A cross section, however, the average power decreases with aspect ratio for $a \leq 0.4$. It may be noted that the average power at $a = 0.4$ is even smaller than that at $a = 1$. The average power at $a = 0.4$ is 1.55 W cm^{-3} with type A cross section, whereas the average power is 1.73 W cm^{-3} for $a = 1$. Similar to type A cross section, the average power is found to decrease with aspect ratio for $a \leq 0.5$ with type B cross section. In addition, type B cross section generally corresponds to smaller average power for all aspect ratios than that at $a = 1$. Therefore, type B cross section may not be suitable for enhanced heating corresponding to regime II.

Figure 4c illustrates the average power distributions for regime III with $R = 2$ cm. It is found that the average power is generally smaller for all aspect ratios than that at $a = 1$ with type A cross section. It is interesting to note that the type B cross section generally corresponds to enhancement of average power for all aspect ratios, and it is observed that the average power decreases with aspect ratio for type B cross sections. The average power for type B cross section is 0.51 W cm^{-3}, whereas the average power is 0.196 W cm^{-3} for type A cross section corresponding to $a = 0.1$. It may also be noted that, the average power is 0.232 W cm^{-3} for $a = 1$. In general, a degree of enhancement for power absorption with type B cross section is larger than that with type A cross section for regime III.

Figure 5a illustrates the grayscale colormap images of microwave power distributions for various aspect ratios (a = 0.1–0.9), with type A cross section corresponding to regime I ($R = 0.5$ cm). The brighter shade denotes the larger magnitudes of microwave power. The maxima corresponding to larger power distributions signify the constructive interference of traveling waves at a resonant situation. It is observed that two brighter zones occur near the left and right faces of the ellipse for $a \leq 0.3$. As the aspect ratio increases beyond 0.4, the brighter shade near the exposed face (left face) tends to disappear, and the regime of high-values of microwave power is to be seen near the right face. It is interesting to note that the strength of the brighter shade at the right face decreases with the increase in aspect ratio. Finally, at a = 0.9 a small region of weaker bright shade at the right face is observed, and the power distribution is similar to the spatial power characteristics for a circular cross section at $a = 1$. The strong resonant situation at very small aspect ratios corresponds to two zones of large microwave power distributions, which result in larger average microwave power at small aspect ratios as seen in Figure 4a.

The colormap images of microwave power distributions for type B cross section corresponding to regime I are shown in Figure 5b. In general, the strength of brighter shade at the right face is quite weak for type B cross sections. This is due to the fact that, the constructive interference of traveling waves is weaker in type B cross sections than that in type A cross section. It is observed that a weaker bright shaded regime occurs at a very small regime near the right face with type B cross section. This results in smaller average power for all aspect ratios as seen in Figure 4a.

Figure 6 shows the distributions of power and temperature (at t = 20 and 60 s) for ellipses with types A and B cross sections, corresponding to regime I with $a = 0.2$. It is observed that for type A cross section, maxima in power occurs near the left and right faces of the ellipse, and the power near the faces vary within 6–7 W cm^{-3}, whereas the central zone has a minima in power (2 W cm^{-3}). Due to larger power absorption at the faces, the temperature enhancement is quite high, and the temperature at the faces reach around 340–345 K during 20 s, and that at the faces reach around 410–420 K at 60 s. Note that, during the entire heating period the central zone reaches around 380 K. On the other hand, the power absorption is quite less for type B cross sections, as also seen in Figure 5. The type B cross section corresponds to a maxima in power at the central regime of the unexposed right face, and the maxima in power is around 2.5 W cm^{-3}, whereas the exposed face corresponds to smaller power absorption (0.5 W cm^{-3}). In contrast, the power absorption for type A cross section varies within 2–7 W cm^{-3}. Due to less power absorption for type B cross section, the temperature varies within 304–316 K during 20 s,

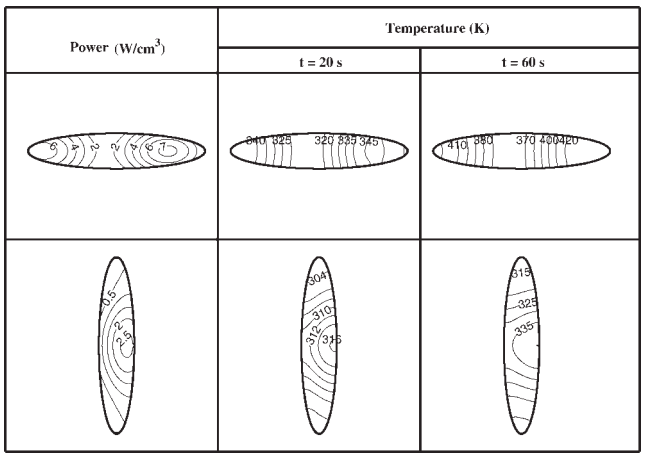

Figure 6. Power and temperature profiles (*t* = 20 and 60 s) of beef samples corresponding to regime I with *a* = 0.2 for type A and B cross sections.

$f = 2450$ MHz, the incident microwave intensity at left face, $I_0 = 1$ W cm^{-2}. It may be noted that both the left and right faces correspond to high-heating rates for type A cross section whereas the central regime at the right face corresponds to high-heating rates for type B cross section.

and 315–335 K during 60 s. For all time intervals, the maxima in temperature is found to occur near the central regime of unexposed right face for type B cross section. Although type A cross section corresponds to larger heating rate, the significant thermal runway occurs due to hot spots near the left and right faces.

Figure 7 shows the distributions of power and temperature (at $t = 20$ and 60 s) for ellipses with types A and B cross sections corresponding to regime I with $a = 0.8$. For both types of cross sections, it is observed that the maxima in absorbed power occurs at the unexposed face. Similar to the previous case with $a = 0.2$, it is found that the maxima in power for type A cross section is larger than that with type B cross section. Note that, the maxima in power for type A cross section is around 3.5 W cm^{-3}, and the maxima in power is around 3 W cm^{-3} for type B cross section. The heating is primarily high near the unexposed face for both types of cross sections. For type A cross section, the temperature varies within 305–320 K during 20 s, and 315–360 K during 60 s. For type B cross section, the temperature varies within 302–318 K during 20 s, and 315–340 K during 60 s. It is interesting to note that the heating rate at the exposed face is quite low irrespective of the type of cross section. Overall, type A cross section may be advantageous for a preferential larger localized heating effect. However, it may be noted that, type A cross section may give larger thermal runaway for large aspect ratios as seen in Figure 7. Therefore spatial-temperature distribution plays a critical role to determine the efficient heating policy for both the limits of aspect ratios.

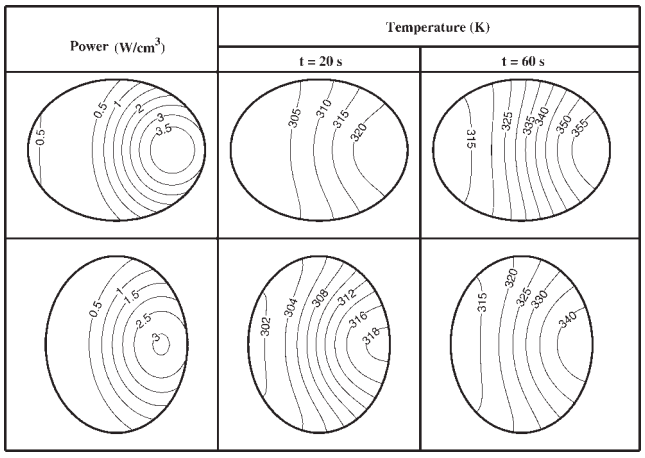

Figure 7. Power and temperature profiles (*t* = 20 and 60 s) of beef samples corresponding to regime I, with *a* = 0.8 for type A and B cross sections.

$f = 2450$ MHz, the incident microwave intensity at left face, $I_0 = 1$ W cm^{-2}. It may be noted that the right face corresponds to high-heating rate for both type A and B cross sections.

Figure 8a illustrates the grayscale colormap images of microwave power distributions for various aspect ratios ($a =$

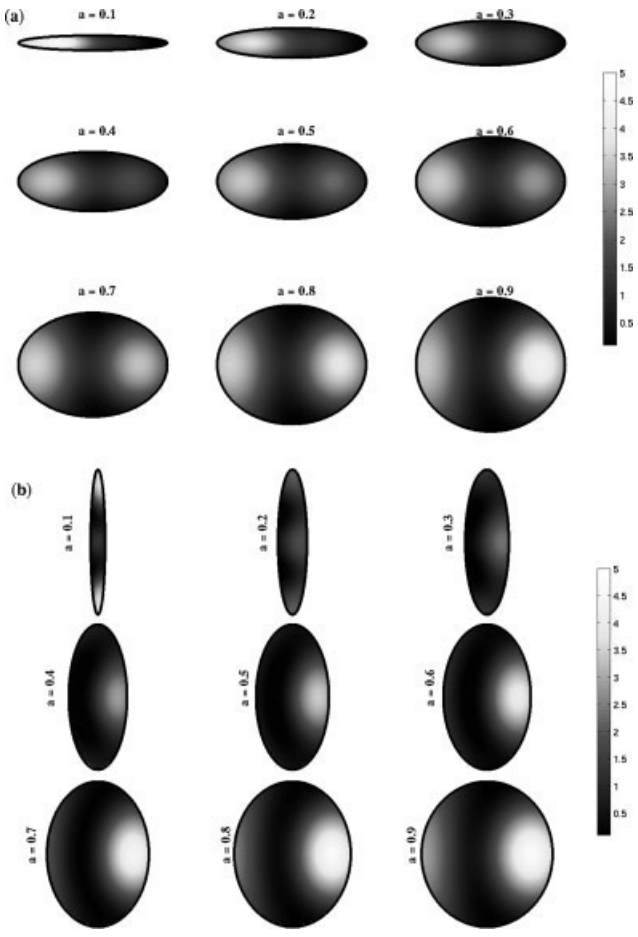

Figure 8. Grayscale colormap images of microwave power distributions in beef samples for various aspect ratios with (a) type A and (b) type B cross sections corresponding to regime II (*R* = 0.67 cm).

$f = 2450$ MHz, the incident microwave intensity at left face, $I_0 = 1$ W cm^{-2}. It may be noted that brighter regime denotes larger power distribution. Two bright regimes near the left and right faces are seen for type A cross section with large-aspect ratios.

Table 2. Generalized Heating Features for Beef Samples with Small and Large Aspect Ratios

Regime I	Regime II	Regime III
Small Aspect Ratio		
• Greater average heating rate is with type A cross section	• Greater average heating rate is with type A cross section	• Greater average heating rate is with type B cross section
• The hot spots occur at both the left and right faces with type A cross section	• The hot spots occur at the left exposed face with type A cross section	• The heating rate is very small with type A cross section, except at the left exposed face
• The central regime has large heating rate with type B cross section	• The top and bottom faces have larger heating rate with type B cross section	• The top and bottom faces have larger heating rate with type B cross section
• Larger thermal gradient is observed with type A cross section	• Larger thermal gradient is observed with type A cross section	• Larger thermal gradient is observed with type A cross section
Large Aspect Ratio		
• Greater average heating rate is with type A cross section	• Greater average heating rate is with type A cross section	• Greater average heating rate is with type B cross section
• The hot spots may occur at the right unexposed face for both types A and B cross sections	• Large heating rates are found at both the left and right faces with type A cross section, and at the right face with type B cross section	• Large heating rates are found at the left face and center with type A and type B cross sections
• Larger thermal gradient is observed with type A cross section	• Larger thermal gradient is observed with type B cross section	• Larger thermal gradient is observed with type A cross section

0.1–0.9), with type A cross section corresponding to regime II ($R = 0.67$ cm). It is observed that one brighter zone occurs at the exposed face for $a = 0.1$–0.4 and two brighter zones are found to occur near the exposed and unexposed faces for $a = 0.8$–0.9. It is interesting to note that the brighter zone at the unexposed face is stronger for $a = 0.8$–0.9. In general, single brighter zone near the exposed face for small aspect ratios would cause the smaller average power and for $a = 0.2$–0.4, the average power is even smaller than that with $a = 1$.

The colormap images for type B cross section corresponding to regime II are shown in Figure 8b. It is interesting to observe that the two brighter zones appear near the top and bottom surfaces with $a = 0.1$, and for $a = 0.2$–0.3, the entire zone is less brighter, which signifies the less power absorption, and that results in smaller average power than that with $a = 1$ as seen in Figure 4b. For $a = 0.4$–0.7, the brighter zone occurs near the unexposed face, and the intensity of brighter zone increases with aspect ratio. At $a = 0.9$, another brighter zone also appears near the exposed face. It is interesting to observe that for $a \geq 0.4$, the increasing intensity of brighter zones with aspect ratio will cause the increasing trend of overall power absorption. The spatial-temperature distributions for aspect ratios have also been computed, and the essential features are summarized in Table 2.

Figure 9a illustrates the grayscale colormap images of microwave power distributions for various aspect ratios ($a = 0.1$–0.9), with type A cross section corresponding to regime III ($R = 2$ cm). It is observed that one brighter zone occurs at the exposed face for $a = 0.1$–0.6, and the brighter zone tends to disappear for $a \geq 0.6$. It is also observed that the brighter zone at the exposed face is stronger for $a = 0.4$, and, therefore, the average power is an increasing function of aspect ratio upto $a \leq 0.4$ for type A cross section. A brighter zone still appears at the central regime for $a = 0.9$, and, hence, the average power is found to be large for high-aspect ratios. Figure 9b illustrates the colormap distribution for type B cross section corresponding to regime III. In general, large number of brighter zones is found to occur for smaller aspect ratios ($a \leq 0.3$), and, therefore, the average power is found to be quite high for $a \leq 0.3$. At high-aspect ratio ($a = 0.9$), the central regime has a brighter zone. However, due to less microwave power absorption at higher aspect ratios, the average power absorption is small. The essential features of spatial-temperature distributions are illustrated in Table 2.

Table 2 summarizes the generalized features of heating characteristics of beef samples, with regimes I, II and III corresponding to radii of circular cross section (R) 0.5, 0.67 and 2 cms, respectively. It is observed that the hot spots leading to high-heating rates generally occur at both the left and right faces, with type A cross section for regime I with small aspect ratios, and this may also result in thermal runaway. In contrast, the type B cross section with regime I is found to give larger heating rates at the central regime. In general, type A cross section with small aspect ratio may be a favored configuration and type B cross section may be recommended for a preferential larger heating of central regime. For large aspect ratios, the hot spots occur at the right face for both type A and B cross sections and larger thermal runaway occurs with type A cross section. For regime II with small aspect ratio, the hot spots at the left face are found with type A cross section, and the top and bottom faces have large heating rates with type B cross section. Similar to regime I with small aspect ratio, type A cross section for regime II also exhibits thermal runaway for small aspect ratios. For large aspect ratio, the large heating rates are found at both the left and right faces with type A cross section, and at the right face with type B cross section. It may be interesting to note that the larger thermal runaway is observed for type B cross section for regime II with large aspect ratio. Overall, type A configuration may be an optimal selection for both regimes I and II. The type B cross section is a favored configuration for large sample dimension corresponding to regime III due to overall larger heating rates. For small aspect ratios, type A cross section may not be recommended, due to very small or negligible heating rates in 80% of the sample, whereas type B cross section corresponds to large heating rates at top and bottom faces. At large aspect ratio, the left exposed face and the central regime correspond to large heating rates for both types A and B cross sections. It may also be noted that type A cross section corresponds to larger ther-

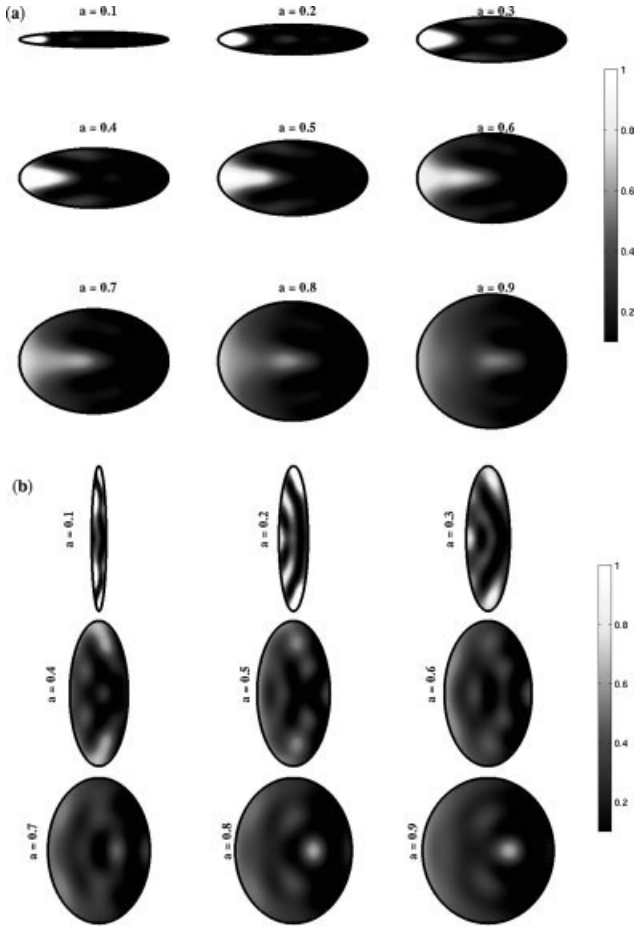

Figure 9. Grayscale colormap images of microwave power distributions in beef samples for various aspect ratios with (a) type A, (b) type B cross sections corresponding to regime III (R = 2 cm).

f = 2450 MHz, the incident microwave intensity at left face, I_0 = 1 W cm^{-2}. It may be noted that brighter regime denotes larger power distribution. In general, larger bright regimes occur for type B cross section.

mal runaway irrespective of aspect ratios. Therefore, type B cross section is a favorable configuration for efficient heating of beef samples with regime III irrespective of aspect ratios.

Microwave heating of oil samples

A preliminary case study on microwave heating of oil samples for cylinders with circular cross sections has been illustrated in Figure 10. The resonances in average power occur at specific sample radius following a relationship as discussed in the previous section and the earlier work.[18] As oil has less dielectric loss, the power absorption in oil samples is in general small. Therefore, the maxima in average power for various resonance modes do not differ significantly. The three regimes (I, II and III) corresponding to various sample radius (R) are considered to investigate further the influence of various elliptical cross sections. It may also be noted that regimes I and II denote resonances, and regime III corresponds to destructive interference for a large sample radius. Note that, the radiuses of the circular cross section (R) are 0.85, 2.5 and 5 cms for regimes I, II and III, respectively. The average power varies within 0.06–0.1 W cm^{-3} for various regimes.

An overall performance on heating effects due to various elliptical cross sections for regimes I–III has been shown via average power vs. aspect ratio plot in Figures 11a–c. Figure 11a illustrates the average power distributions for regime I corresponding to R = 0.85 cm. It has been observed that the average power is almost invariant with various aspect ratios, except for very small aspect ratios. Figure 11b illustrates the average-power distribution for regime II with R = 2.5 cm. It is observed that the average power is high (0.133 W cm^{-3}) for a = 0.1 with type A cross section, and average power decreases with aspect ratio. Note that, the average power is 0.079 W cm^{-3} at a = 1. It may also be noted that the average power at regime II with type A cross section for small aspect ratios (a = 0.3), is greater than that at regime I with all aspect ratios. Therefore, it may be concluded that a sample with larger R corresponding to regime II, may be processed faster than samples with smaller R corresponding to regime I for specific aspect ratios. It may also be noted that, the average power is found to increase with aspect ratio for type B cross section with $a \geq 0.4$ as seen in Figure 11b. Figure 11c illustrates average power distributions for regime III with R = 5 cm. The regime III is chosen as a representative of a large sample. Similar to regime II, it is observed that the average power decreases with aspect ratio for type A cross section and the average power increases with aspect ratio for type B cross section. The average power varies within 0.086–0.058 W cm^{-3} for type A cross section, whereas the average power varies within 0.044–0.058 W cm^{-3} for type B cross section corresponding to regime III.

The detailed analysis on power and temperature distributions for various aspect ratios, and types of cross sections are not shown for all regimes. Identical average heating and

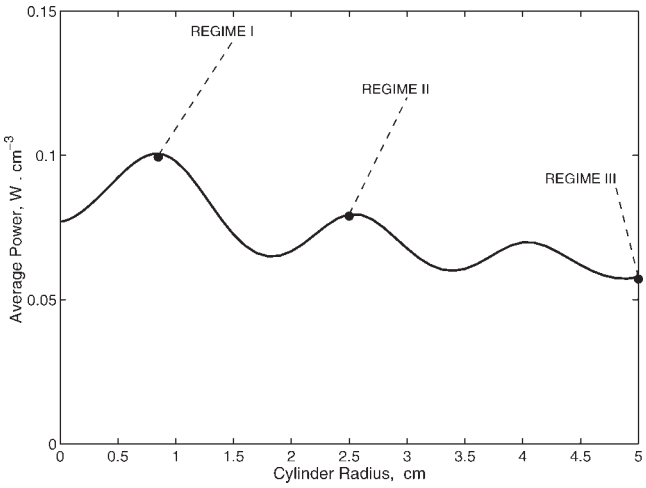

Figure 10. Average power (W · cm^{-3}) vs cylinder radius (cm) for oil samples.

f = 2450 MHz, the incident microwave intensity at left face, I_0 = 1 W cm^{-2}. The regimes I and II correspond to maxima in average power, and regime III represents a minima in average power.

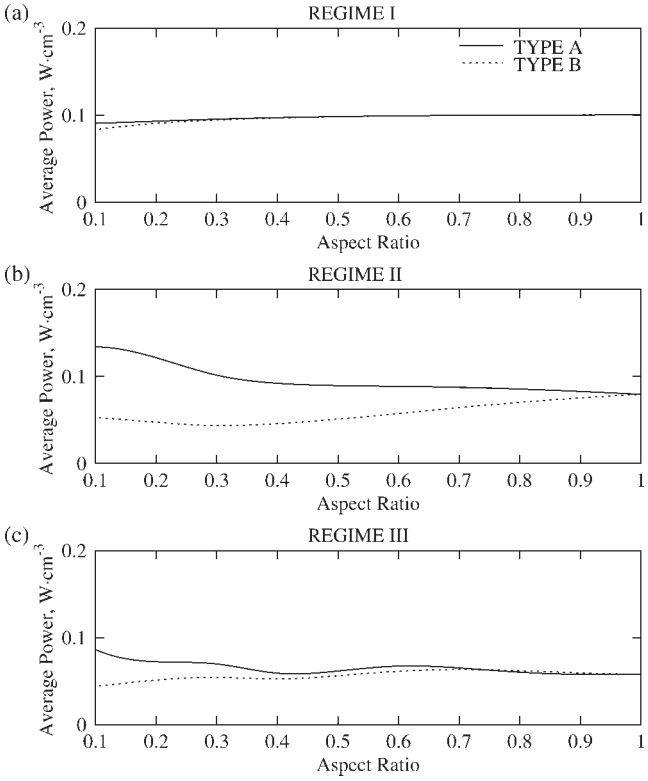

Figure 11. Average power (W · cm^{-3}) vs. aspect ratio for oil samples with (a) regime I, (b) regime II, and (c) regime III.

f = 2,450 MHz, the incident microwave intensity at left face, I_0 = 1 W cm^{-2}. The average power is invariant with types of cross sections for regime I, whereas the average power is larger with type A cross section for regimes II and III.

spatially uniform heating characteristics are observed for regime I with type A/B cross sections for all aspect ratios. A representative detailed analysis of spatial power and temperature distributions for regime II will be discussed next. The heating features for regime III are almost similar to regime II, and essential heating characteristics are highlighted in Table 3.

Figure 12a illustrates the grayscale colormap images of microwave power distributions for various aspect ratios (a = 0.1–0.9) with type A cross section corresponding to regime II (R = 2.5 cm). It is observed that almost the entire zone is bright for a = 0.1, and that signifies overall high-power absorption for a = 0.1. It may be noted that, a very small regime of the exposed left face corresponds to small power deposition or darker shaded regime. As a consequence, the average power for a = 0.1 is quite high as seen in Figure 11b. The area under the brighter shaded regime attached with the right unexposed face is decreased with the increase in aspect ratio. At a = 0.3, the brighter regime is split into two regimes occurring at the unexposed face and the central regime. The brighter shade at the central regime gradually moves toward the left exposed face as the aspect ratio increases. It is also interesting to note that the intensity of brightness of the left bright regime decreases with aspect ratio. Overall the effective area of brightest regime decreases with aspect ratio, and that results in decreasing trend of average power with aspect ratio as seen in Figure 11b.

The colormap images of microwave power distributions for type B cross section are shown in Figure 12b. In general, the strength of bright shade is very weak for small aspect ratios ($a \leq 0.3$). Hence, the average power is quite small with smaller aspect ratios as seen in Figure 11b. A brighter shade gradually appears near the unexposed face as aspect ratio increases, and the brightness or the power absorption increases with aspect ratio. Therefore, the average power is also enhanced at high-aspect ratio as seen in Figure 11b.

Figure 13 shows the distributions of power and temperature (at t = 40 and 100 s) for ellipses with types A and B cross sections with a = 0.2. It is observed that for type A cross section, maxima in power occurs near the central regime and the right unexposed face. A minima in power absorption occurs near the left exposed face. It is also observed that the overall spatial power absorption varies within 0.08–0.16 W cm^{-3} due to low-dielectric loss of oil. During 40 s, the temperature varies within 301.5–304.5 K, and at t = 100 s, the temperature varies within 304–312 K.

Table 3. Generalized Heating Features for Oil Samples with Small and Large Aspect Ratios

Regime I	Regime II	Regime III
Small Aspect Ratio		
● Identical average heating rate occurs with types A and B cross sections	● Greater average heating rate is with type A cross section	● Greater average heating rate is with type A cross section
● Almost uniform heating occurs within sample for both types A and B cross sections	● The hot spots occur at the right unexposed face with type A cross section	● Large heating rates are found at the central regime with type A cross section
	● The top and bottom faces have larger heating rate with type B cross section	● The top and bottom faces have larger heating rate with type B cross section
	● Larger thermal gradient is observed with type A cross section	● Larger thermal gradient is observed with type A cross section
Large Aspect Ratio		
● Identical average heating rate occurs with types A and B cross sections	● Greater average heating rate is with type A cross section	● Identical average heating rate occurs with types A and B cross sections
● Almost uniform heating occurs within sample for both types A and B cross sections	● Large heating rates are found at right face with both types A and B cross sections	● Large heating rates are found at right face with both types A and B cross sections
	● Identical thermal gradient is observed with both types A and B cross sections	● Identical thermal gradient is observed with both types A and B cross sections

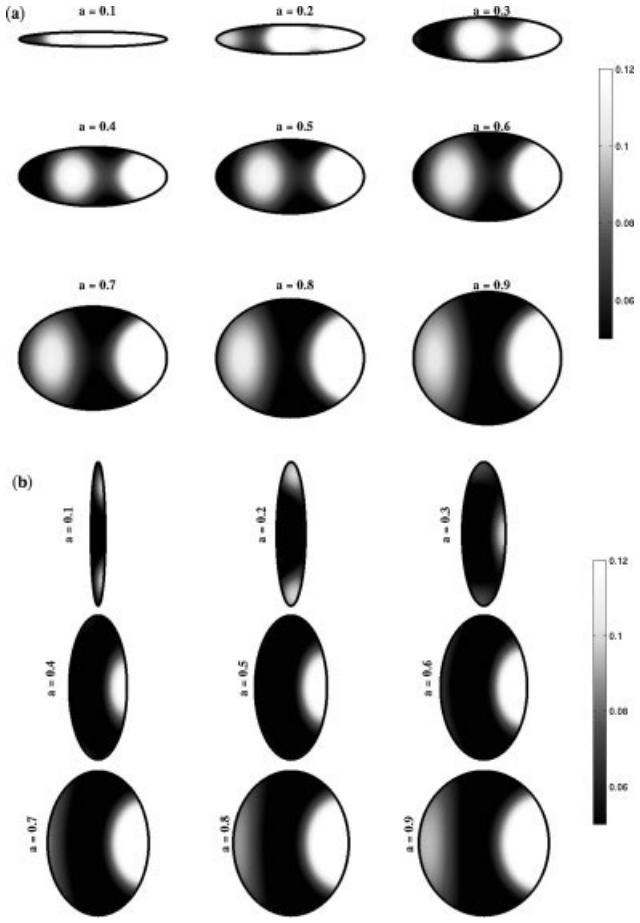

Figure 12. Grayscale colormap images of microwave power distributions in oil samples for various aspect ratios with (a) type A, (b) type B cross sections corresponding to regime II (R = 2.5 cm).

f = 2450 MHz, the incident microwave intensity at left face, I_0 = 1 W cm^{-2}. It may be noted that brighter regime denotes larger power distribution. In general, two bright regimes at both the left and right faces occur for type A cross section, whereas stronger bright regime at the right face occurs for type B cross section with larger aspect ratio.

The overall power absorption is less for type B cross section at a = 0.2. The power absorption varies within 0.01–0.09 W cm^{-3}, and the maxima in power occurs at a very small regime near the top and bottom faces. The temperature varies within 300.5–302 K during 40 s, and the temperature varies within 301–305 K during 100 s for type B cross section. Overall, type A cross section gives a larger heating rate with a larger thermal runaway.

Figure 14 shows the distributions of power and temperature (at t = 40 and 100 s) for ellipses with types A and B cross sections with a = 0.8. It is observed that the primary maxima is 0.2 W cm^{-3} at the unexposed right face, and the secondary maxima in microwave power is around 0.1 W cm^{-3} occurring at the exposed face with type A cross section. During 40 s and 100 s, the temperature variations are 302–304.5 K and 304–310 K, respectively. It may be noted that the heating rates are slightly higher with a = 0.2 for type A cross section, as seen in Figure 13. The type B cross section shows similar heating patterns with that of type A cross section, as seen in Figure 14. The maxima in temperature are observed at the unexposed face for both t = 40 s and 100 s. It is interesting to note that overall thermal gradient is identical for type A and B cross section with large aspect ratios.

Table 3 illustrates the generalized features of heating characteristics of oil samples with regimes I, II and III corresponding to radii of circular cross section (R) 0.85, 2.5 and 5 cms, respectively. In general, the average power absorption in oil samples is much smaller than beef samples for all sample dimensions due to small dielectric loss of oil. It is also observed that the average power or heating rate is invariant with aspect ratios for regime I irrespective of type A/B cross section. It is also interesting to note that the uniform heating is observed throughout the sample domain for all types of cross sections with regime I. Therefore, the sample dimension corresponding to regime I is definitely an optimal choice of heating. The greater average heating rate is observed with type A cross section for regime II irrespective of types of cross sections. At small aspect ratio, the hot spots are found to occur at the right unexposed face and thermal runaway is observed with type A cross section, whereas type B cross section may result in larger heating rate at top and bottom faces; however, thermal runway can be avoided with type B cross section. At large aspect ratio, both the types of cross sections correspond to larger heating rate at the right face, and significant thermal runaway is not observed for both type cross sections. Overall, type A cross section is a very optimal choice for regime II. The greater average heating rate is observed with type A cross section for regime III with small aspect ratios. The central regime and top/bottom face have larger heating rates with types A and B cross sections, respectively with small aspect ratio. However, larger thermal runway is seen for type A cross section with small aspect ra-

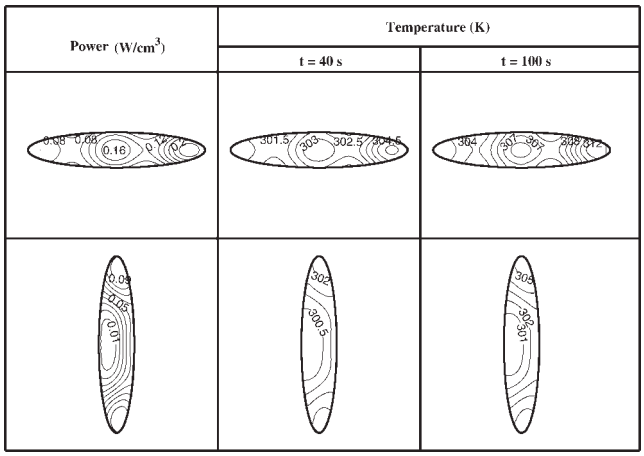

Figure 13. Power and temperature profiles (t = 40 and 100 s) of oil samples corresponding to regime II with a = 0.2 for type A and B cross sections.

f = 2450 MHz, the incident microwave intensity at left face, I_0 = 1 W cm^{-2}. It may be noted that the overall heating rate is larger with type A cross section.

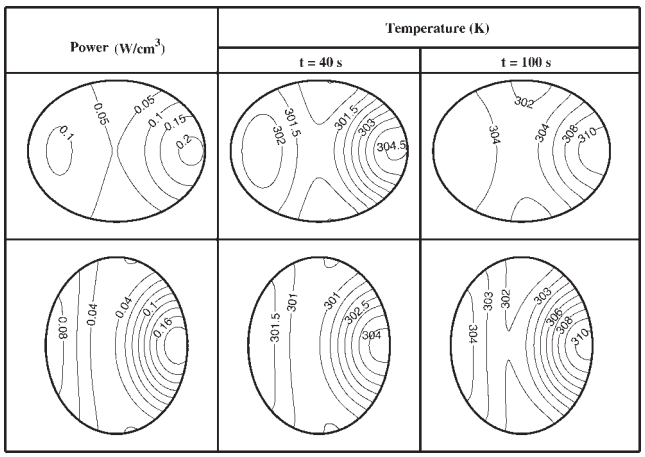

Figure 14. Power and temperature profiles (t = 40 and 100 s) of oil samples corresponding to regime II with a = 0.8 for type A and B cross sections.

f = 2450 MHz, the incident microwave intensity at left face, I_0 = 1 W cm^{-2}. Identical heating rates are observed for both types of cross sections.

tio for regime III. Identical average heating rate or thermal runaway is observed irrespective of types of cross sections for large aspect ratio with regime III. Therefore, large samples with large aspect ratios with either types of cross section corresponding to regime III can be optimal choices for efficient microwave heating of oil samples.

Conclusion

An extensive study has been carried out to investigate the role of various elliptical cross sections on microwave heating of 2-D cylinders of beef (high-dielectric loss) and oil (low-dielectric loss). The case studies are shown for various regimes, based on samples with circular cross section. The regimes are selected based on maxima or minima in average power, and various sample dimensions with circular cross sections. The analysis was done with a prime interest on the enhancement or focusing of microwave power within a sample via varying the cross section with different aspect ratios. The generalized features on heating characteristics are highlighted for various limits of aspect ratios as shown in Tables 2 and 3.

The case studies for two materials with high-and low-dielectric losses have been illustrated for various regimes with type A and type B cross sections. It is observed that choice of type A /type B configuration depends primarily on material dielectric properties and various regimes (I–III). Efficient heating based on "larger heating rate" and "optimal thermal runaway" is found to be strongly dependent on type A/B configuration, and the configuration plays a critical role on interference of waves leading to desired heating characteristics, which has been established for the first time in this work. The proposed finite-element simulation strategy is quite robust, which can be suitably extended for various realistic shapes. Current simulation studies may also provide useful guidelines on efficient processing for materials with various ranges of dielectric properties.

Notation

a = aspect ratio
A_c = cross sectional area of the cylinder, m^2
c = velocity of light, m s^{-1}
C_p = specific heat, J kg^{-1} K^{-1}
D_p = penetration depth, m
E_x = electric field intensity, V m^{-1}
E_0 = incident electric field intensity, V m^{-1}
f = frequency, Hz
$\mathbf{J}$ = Jacobian
k = thermal conductivity, W m^{-1} K^{-1}
q = microwave source term
Q = dimensionless microwave source term, W m^{-3}
R = radius of the circular sample, m
R_h = radius of the hypothetical circular domain, m
$\mathbf{R}$ = Residual
t = time, s
T = temperature, K
u_x = dimensionless electric field
v_x = dimensionless real field component
w_x = dimensionless imaginary field component

Greek letters

γ = dimensionless propagation constant
λ_m = wavelength, m
ε_0 = free space permittivity, Farad m^{-1}
θ = dimensionless temperature
κ' = relative dielectric constant
κ'' = relative dielectric loss
ρ = density, kg m^{-3}
τ = dimensionless time
ψ = basis functions
ω = angular frequency, Rad s^{-1}
Γ_1 = sample boundary
Γ_2 = hypothetical boundary in free space

Acknowledgments

Author would like to thank anonymous reviewers for critical comments and suggestions which are helpful to improve the quality of the manuscript. Author also acknowledges the assistance of Dr. M. Bhattacharya for computations of grid generation.

Literature Cited

1. Weil CM. Absorption characteristics of multilayered sphere models exposed to UHF/Microwave Radiation. *IEEE Trans Biomed Eng*. 1975;BME-22:468–476.
2. Ayappa KG, Davis HT, Davis EA, Gordon J. Two – dimensional finite element analysis of microwave heating. *AIChE J*. 1992;38: 1577–1592.
3. Chatterjee A, Basak T, Ayappa KG. Analysis of microwave sintering of ceramics. *AIChE J*. 1998;44(10):2302–2311.
4. Chamchong M, Datta AK. Thawing of foods in a microwave oven: I. effect of power levels and power cycling. *J Microwave Power and EM Energy*. 1999;34:9–21.
5. Basak T, Ayappa KG. Analysis of microwave thawing of slabs with effective heat capacity method. *AIChE J*. 1997;43(7):1662–1674.
6. Basak T, Ayappa KG. Influence of internal convection during microwave thawing of cylinders. *AIChE J*. 2001;47(4):835–850.
7. Zhang H, Datta AK, Taub IA, Doona C. Electromagnetics, heat Transfer, and thermokinetics in microwave sterilization. *AIChE J*. 2001;47:1957–1968.
8. Sivalingam G, Agarwal N, Madras G. Kinetics of microwave-assisted oxidative degradation of polystyrene in solution. *AIChE J*. 2003;49:1821–1826.
9. Lee MZC, Marchant TR. Microwave thawing of cylinders. *Applied Math Modeling*. 2004;28(8):711–733.
10. Ohlsson T, Risman PO. Temperature distribution of microwave heating-spheres and cylinders. *J Microwave Power*. 1978;13:303–310.

11. Massoudi H, Durney CH, Barber PW, Iskander MF. Electromagnetic absorption in multilayered cylinder models of man. *IEEE Trans. Microwave Theory and Techniques*. 1979a;27:825–830.
12. Massoudi H, Durney CH, Johnson CC. A geometrical-optics and an exact solution for internal fields in and energy absorption by a cylindrical model of man irradiated by an electromagnetic plane wave. *Radio Sci*. 1979b;14:35–42.
13. Ruppin R. Electromagnetic power deposition in a dielectric cylinder in the presence of a reflecting surface. *IEEE Trans Microwave Theory and Techniques*. 1979;27:910–914.
14. Schlunder EU. Microwave drying of ceramic spheres and cylinders. *Chemical Engineering Research & Design*. 1993;71(A6):622–628.
15. Ayappa KG, Davis HT, Crapiste G, Davis EA, Gordon J. Microwave heating: an evaluation of power formulations. *Chem Eng Sci*. 1991; 46:1005–1016.
16. Basak T, Ayappa KG. Role of length scales on microwave thawing dynamics in 2D cylinders. *Int J Heat and Mass Transfer*. 2002;45:4543–4559.
17. Basak T. Analysis of resonances during microwave thawing of slabs. *Int J Heat and Mass Transfer*. 2003;46:4279–4301.
18. Ayappa KG, Davis HT, Barringer SA, Davis EA. Resonant microwave power absorption in slabs and cylinders. *AIChE J*. 1997;43: 615–624.
19. Ayappa KG. Resonant microwave power absorption in slabs. *J Microwave Power and E M Energy*. 1999;34:33–41.
20. Basak T, Kumaran SS. A generalized analysis on material invariant characteristics for microwave heating of slabs. *Chem Eng Sci*. 2005; 60(20):5480–5498.
21. Basak T. Role of resonances on microwave heating of oil-water emulsions. *AIChE J*. 2004;50(11):2659–2675.
22. Fowler AJ, Bejan A. The effect of shrinkage on the cooking of meat. *Int J Heat and Fluid Flow*. 1991;12(4):375–383.
23. Keller JB, Givoli D. Exact non-reflecting boundary-conditions *J Computational Phys*. 1989;82(1):172–192.
24. Reddy JN. An Introduction to the Finite Element Method. New York: McGraw-Hill, 1993.

Manuscript received Nov. 9, 2006, and revision received Feb. 13, 2007.